

Revisiting mandibular symphyseal shape in juvenile early hominins and modern humans using a deformation-based approach

Veronika A. Zimmer^{a,*}, Anna Oettlé^b, Jakobus Hoffmann^c, John Francis Thackeray^d, Bernhard Zipfel^d, José Braga^{d,e}

^aSchool of Computation, Information and Technology, Technical University of Munich, Boltzmannstraße 3, 85748 Garching, Germany

^bSefako Makgatho Health Sciences University, Pretoria, South Africa

^cSouth African Nuclear Energy Corporation (Necsa), Pretoria, 001, South Africa

^dEvolutionary Studies Institute, University of the Witwatersrand, PO WITS, Johannesburg, 2050, South Africa

^eCentre d'Anthropobiologie et de Génomique de Toulouse, Université Paul Sabatier Toulouse III, Faculté de Médecine Purpan, 37 Allées Jules Guesde, 31000 Toulouse, France

*Corresponding author; e-mail: veronika.zimmer@tum.de

ORCID iDs: Zimmer: 0000-0002-5093-5854; Oettlé: 0000-0002-5665-6581;

Hoffmann: 0000-0002-8206-3966; Thackeray: 0000-0001-6884-382X;

Zipfel: 0000-0002-4251-884X; Braga: 0000-0002-8483-076X

Supplementary material

Text S1. Diffeomorphic Shape Matching using *deformetrica*

The deformation between shapes can be described by the action of diffeomorphisms, smooth and invertible functions that align two shapes by deforming the underlying domain. This is realized by placing a regular grid of N_p control points $(q_i)_{i=1,\dots,N_p}$ over the meshes. Vectors $(\mu_i)_{i=1,\dots,N_p}$, called momenta, are attached to each control point. Together the control points and momenta parameterize the diffeomorphism, which is modelled as a vector field

$$X(x) = \sum_{i=1}^{N_p} K(x, q_i) \cdot \mu_i. \quad I$$

Here, $X(x)$ is the vector field at position $x \in \mathbb{R}^d$, $d \in \{2,3\}$ and $K(x_1, x_2) = \exp(-\frac{\|x_1 - x_2\|^2}{\sigma^2})$ is a Gaussian Kernel with width σ . During the matching procedure, the underlying space is deformed by optimizing the positions of the control points q_i and the momenta μ_i to align a shape S_j to a reference shape T . The output of the DSM using *deformetrica* is the control points and deformation momenta, describing the amount of deformation necessary to align the shapes. In the following, we denote the optimized momenta by the matrix $M \in \mathbb{R}^{N_p, d}$, where d is the dimension of the underlying space (here: $d=2$ for the chin profile and $d=3$ for the chin surface), and N_p the number of control points.

We employed and compared two algorithms implemented in *deformetrica*: (i) deterministic atlas construction, and (ii) pairwise registrations. Given a set $\mathcal{S} = \{S_i\}_{i=1,\dots,N_s}$ of N_s shape. For the atlas construction, each shape is aligned to an a priori defined template shape T . We interpreted the deformation momenta M_i from shape S_i to the template as coordinates in shape space. Using the pairwise registration, we performed pairwise shape matching between all pairs of shapes in \mathcal{S} . We interpreted the resulting deformation momenta M_{ij} between shapes S_i, S_j as a notion of pairwise distances.

Both approaches have their limitations. To construct a deterministic atlas, an unbiased template T must exist and has to be created (see figs. 1 and 2), which is not a straightforward task. Then, with an appropriate template, N_s registrations for a population of N_s shapes are performed. Employing pairwise registrations overcomes the difficulty of defining a template shape.

However, instead of only N_s registrations to construct an atlas, $\frac{N_s(N_s-1)}{2}$ registrations are necessary to align all pairs. This makes the pairwise approach computationally more demanding. The most important hyperparameters for a successful shape matching are the kernel size σ_W for the computations of the metric for optimization (see [Durrleman, et al., 2014] for a detailed explanation) and the number of control points. The control points are initialized with spacing σ from Eq. (1). We empirically selected $\sigma_W = 8 \text{ mm}$ and $\sigma = 3 \text{ mm}$ in all experiments, which resulted in $N_p = 30$ control points for the profile in 1D and $N_p = 180$ control points for the surface in 2D.

Text S2. Kernel Principal Component Analysis for dimensionality reduction

The deformation momenta provide the most important information for statistical analysis as they describe the amount of deformation between two shapes, either momenta M_i for specimen shape S_i and template shape T (atlas), or momenta M_{ij} for two specimens' shapes S_i and S_j (pairwise).

We applied non-linear Kernel Principal Component Analysis (kPCA) (Schölkopf, 1998) to the deformation momenta to identify the principal modes of variation. The output provides new coordinates in a low-dimensional embedding space, which is analyzed to find cluster in the data with similar shape. In particular, kPCA maps a high-dimensional input

manifold to a lower-dimensional output manifold using the so-called *kernel-trick*. Given a data matrix $X \in \mathbb{R}^{N,p}$ with N data points $x_i \in \mathbb{R}^p$ of dimension p . kPCA finds a representation $Y^{N,q}, q < p$, by transforming the input data nonlinearly onto a feature space F using the mapping $\Phi: \mathbb{R}^p \rightarrow F$. This mapping is never computed explicitly, but described by a kernel function representing the inner product in the feature space. The kernel matrix $K = (K_{ij})_{i,j=1,\dots,N}$ is given by

$$K_{ij} = k(x_i, x_j) = \langle \Phi(x_i), \Phi(x_j) \rangle = \Phi(x_i) \cdot \Phi(x_j)^T$$

and its eigenvalues are used to find the low dimensional embedding (comparable to standard PCA).

ATLAS APPROACH

We collect the deformation momenta M_i for all shapes $S_i, i = 1, \dots, N_s$, in a momenta matrix $\mathcal{M} \in \mathbb{R}^{N_s, d \cdot N_p}$, where the i th row of \mathcal{M} are the linearized momenta M_i for the alignment of S_i to template T with $\mathcal{M}_i = [\mu_{i,1}^{(1)}, \dots, \mu_{i,1}^{(d)}, \mu_{i,2}^{(1)}, \dots, \mu_{i,2}^{(d)}, \dots, \mu_{i,N_p}^{(1)}, \dots, \mu_{i,N_p}^{(d)}] \in \mathbb{R}^{d \cdot N_p}$ and momenta $\mu_{i,n} = (\mu_{i,n}^{(1)}, \dots, \mu_{i,n}^{(d)}) \in \mathbb{R}^d$ of control point q_n . kPCA is then performed on the momenta matrix \mathcal{M} using a kernel of radial basis functions.

PAIRWISE APPROACH

In contrast to the atlas approach, the pairwise approach does not yield a set of momenta for each shape, but for each pair of shapes. Therefore, it is not possible to apply kPCA as described in the previous paragraph. Instead, we compute directly the kernel matrix K using

$$K_{ij} = \exp(-\gamma \cdot d_{ij}) \quad \text{with distance} \quad d_{ij} = \frac{1}{N_p} \sum_{n=1}^{N_p} \|\mu_{ij,n}\|^2 \quad \text{for momenta} \quad \mu_{ij,n} =$$

$$\left(\mu_{ij,n}^{(1)}, \dots, \mu_{ij,n}^{(d)}\right) \in \mathbb{R}^d, n = 1, \dots, N_p.$$

For both approaches, we obtain an output matrix $\mathcal{Y} \in \mathbb{R}^{N_s, q}$ of new coordinates $y_i \in \mathbb{R}^q, i = 1, \dots, N_s$ for each shape S_i . We selected $q = 5$ output dimensions in all experiments.

We analyzed the new representations y_i of shapes $S_i, i = 1, \dots, N_s$ regarding their ability to distinguish and capture different properties of the samples, such as taxon, sex, age (sex and age only for the modern human sample).

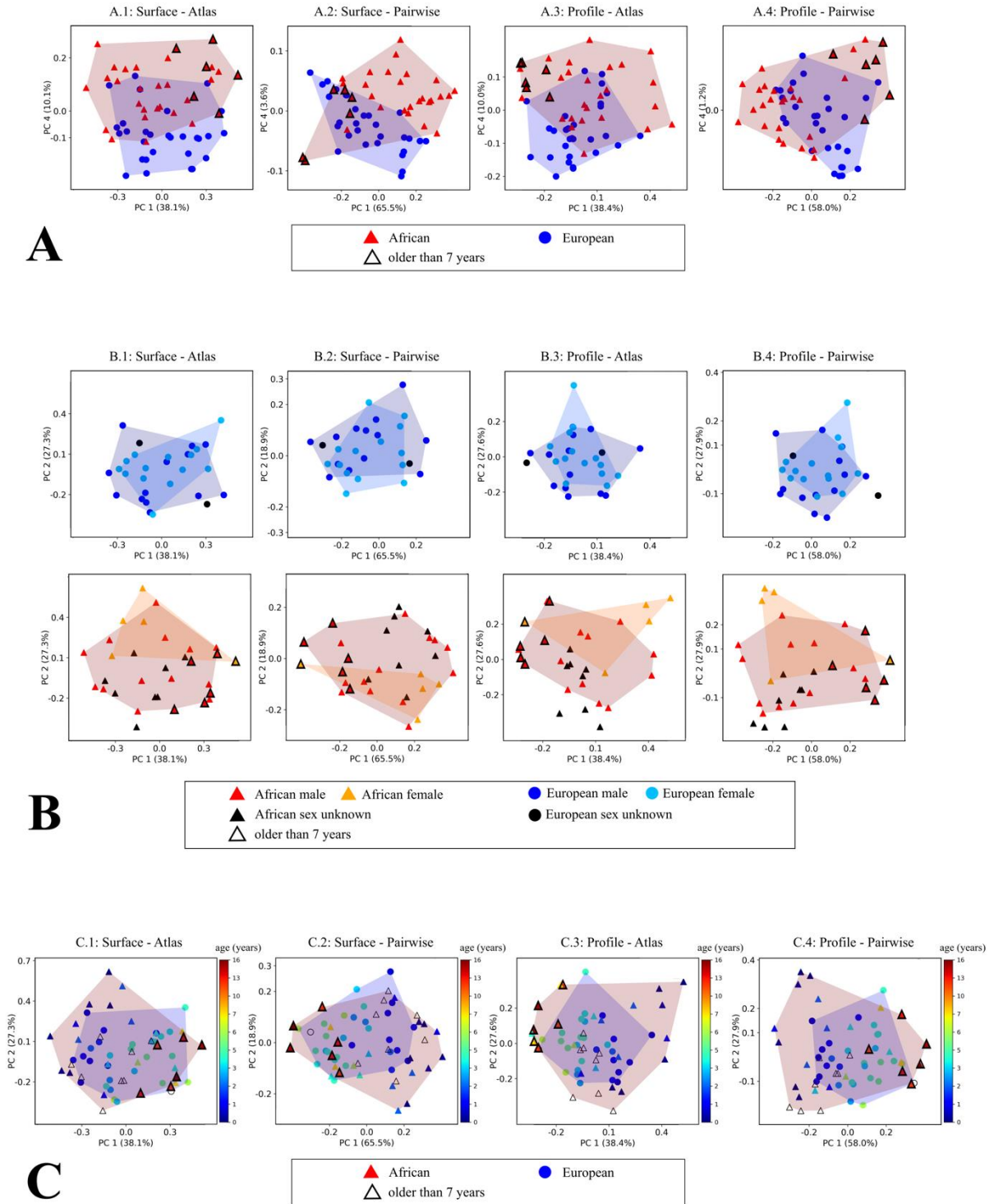


Figure S2. Modern human sample. Plot of principal components obtained by kernel PCA using the atlas and pairwise approach on the symphyseal surface and midsagittal profile. A: Most predictive dimension for group differences. Plot of the first and fourth (most predictive for geographical origin) principal component. Colour coding according to African (red) and

European (blue). B: Sex-type differences. Plot of the first two principal components. Colour coding according to male (red, blue) and female (orange, light blue). C: Shape and age: Plot of the first two principal components. Colour coding according to age in years.

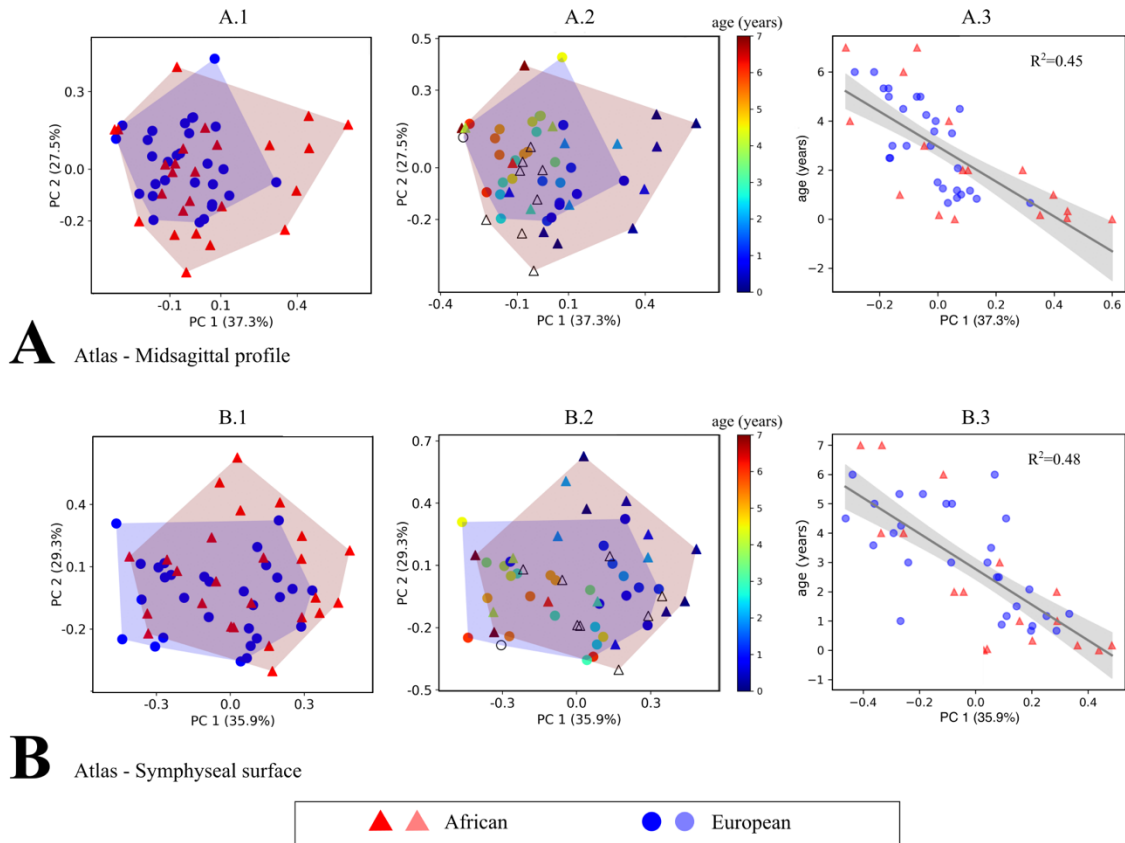
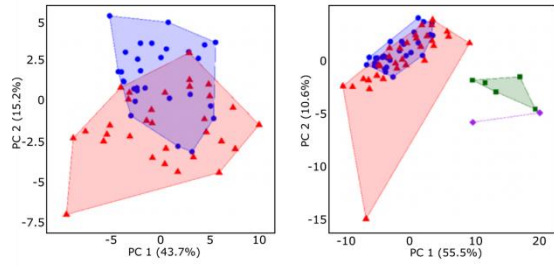
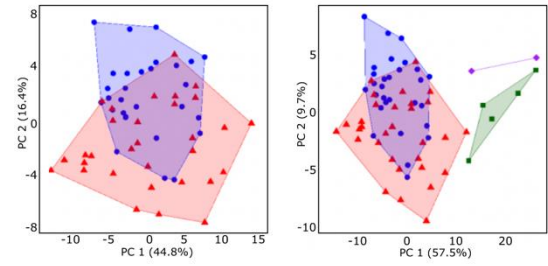


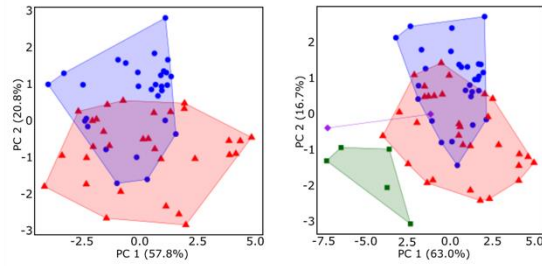
Figure S2. Modern human sample with age distribution from neonate to 7 years. (A.1-2; B.1-2) Plot of the first two principal components obtained by kernel PCA using the atlas approach on the symphyseal surface (A) and midsagittal profile (B). Individuals older than 7 years are excluded from this analysis, but still a larger variation can be observed in the African sample (red) compared to the European sample (blue) with a percentage difference of 24.4% on the surface and 64.3% on the profile. (A.3, B.3) Linear regression of the first principal component with the age (in years).



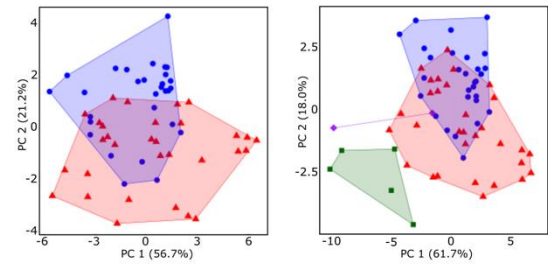
A Symphyseal surface: 60 landmarks



B Symphyseal surface: 120 landmarks



C Midsagittal profile: 15 landmarks



D Midsagittal profile: 30 landmarks

Figure S3. GMM plots of first two principal components. Binary plots of the first two dimensions from a Principal Component Analysis after a Generalized Procrustes Analysis of 60 and 120 semi-landmarks on the symphyseal surface (A, B, respectively) or 15 and 30 semi-landmarks of the midsagittal profile (C, D, respectively). Red triangles and blue circles are for European and African modern humans, respectively. Green squares and purple diamonds are for *Paranthropus robustus* and *Australopithecus africanus*, respectively.

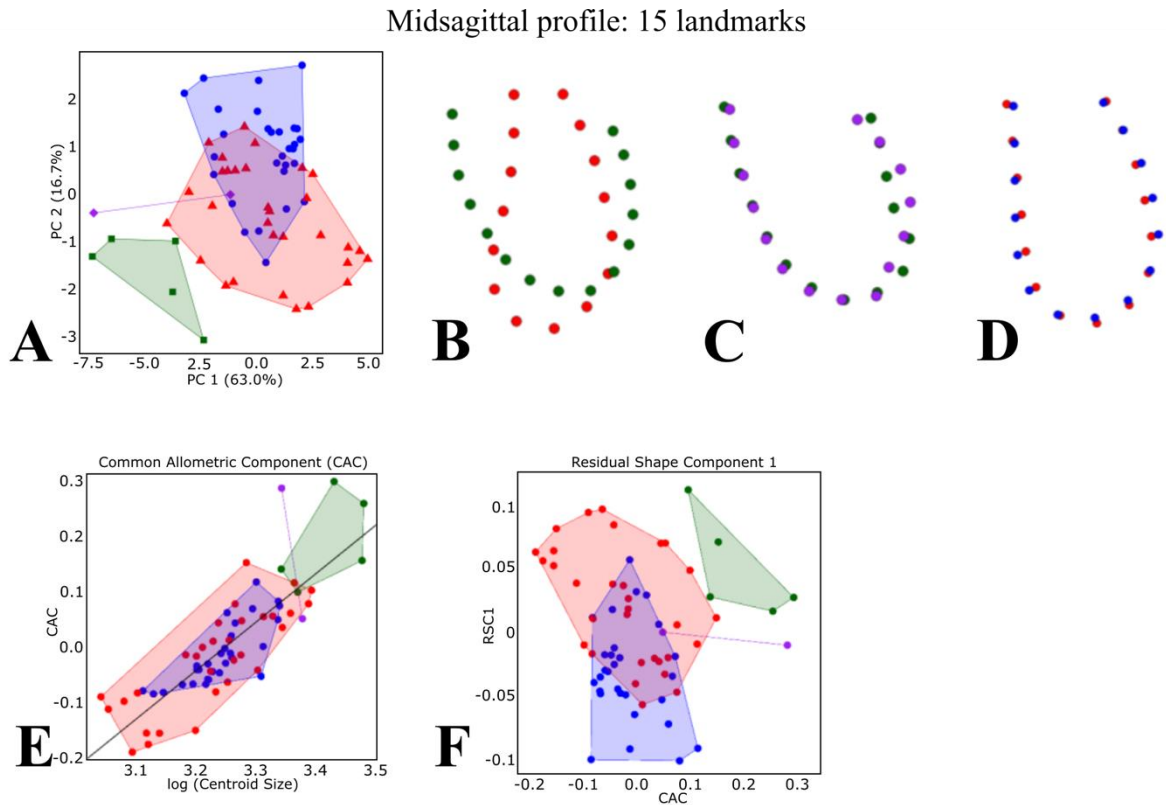


Figure S4. GMM analysis of the midsagittal profile. (A) Binary plot of the first two dimensions from a Principal Component Analysis after a Generalized Procrustes Analysis of 15 semilandmarks located on the midsagittal profile (2D). Red triangles and blue circles are for European and African modern humans, respectively. Green squares and purple diamonds are for *Paranthropus robustus* and *Australopithecus africanus*, respectively. (B) Difference between the semilandmark configurations of the minimum (green) and maximum (red) values along PC1 in the shape space (A). (C) Difference between the mean shapes of *A. africanus* (purple) and *P. robustus* (green). (D) Difference between the mean shapes of modern humans from Europe (blue) and Africa (red). (E) Significant linear correlation between shape differences caused by allometry (or Common Allometric Component, CAC) and centroid size (CS). (F) Relationship between shape differences caused by allometry (CAC) those that are not (or Residual Shape Component, RSC1).

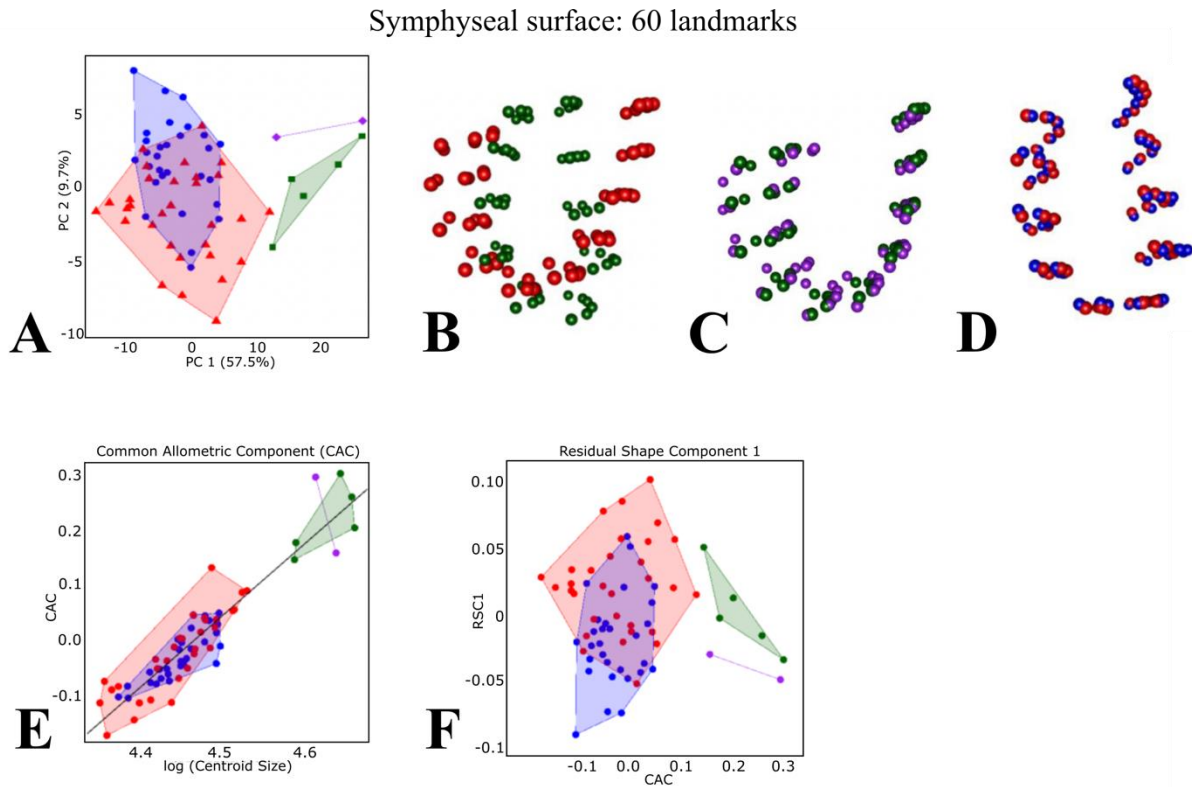
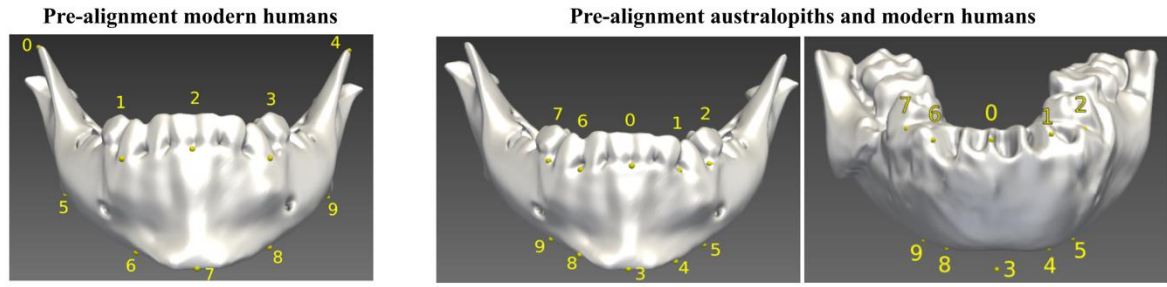
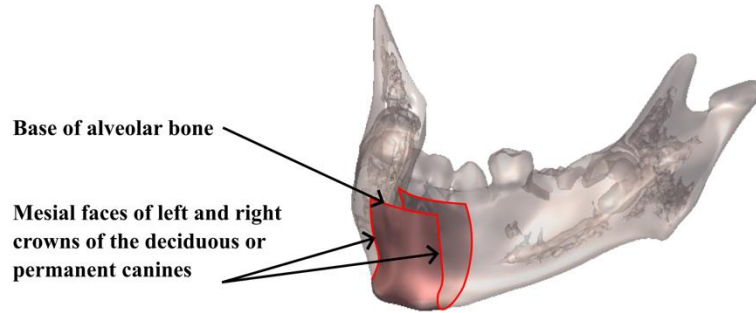


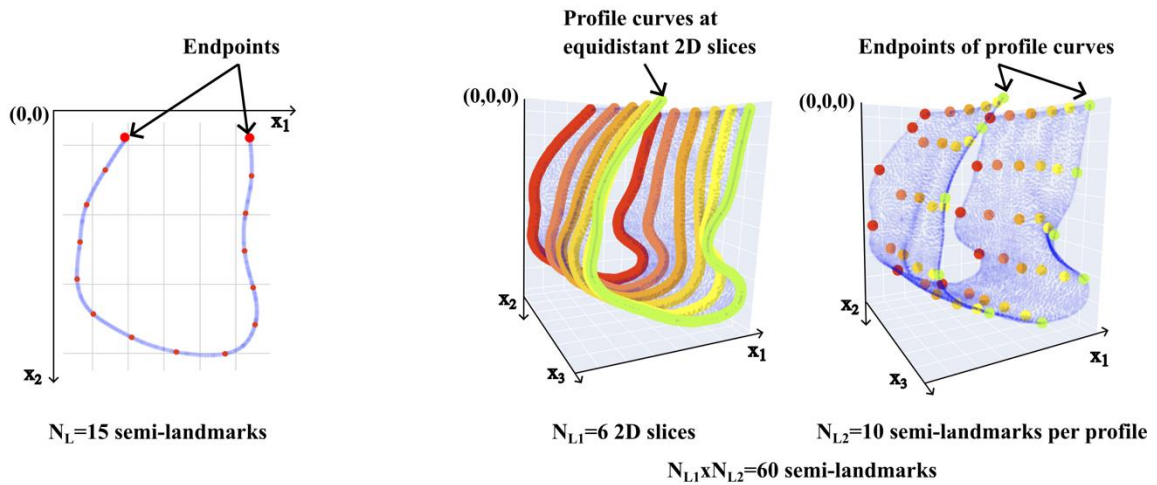
Figure S5. GMM analysis of the symphyseal surface. (A): Binary plot of the first two dimensions from a Principal Component Analysis after a Generalized Procrustes Analysis of 60 semilandmarks located on the symphyseal surface (3D). Red triangles and blue circles are for European and African modern humans, respectively. Green squares and purple diamonds are for *Paranthropus robustus* and *Australopithecus africanus*, respectively. (B) Difference between the semilandmark configurations of the minimum (red) and maximum (green) values along PC1 in the shape space (A). (C) Difference between the mean shapes of *A. africanus* (purple) and *P. robustus* (green). (D) Difference between the mean shapes of modern humans from Europe (blue) and Africa (red). (E) Significant linear correlation between shape differences cause by allometry (or Common Allometric Component, CAC) and centroid size (CS). (F) Relationship between shape differences caused by allometry (CAC) those that are not (or Residual Shape Component, RSC1).



A Landmark placement for global mesh alignment



B Region of interest extraction



C Semi-landmark extraction

Figure S6. Illustration of pre-processing steps. (A): Landmarks for global mesh alignment in the pre-processing. 10 Landmarks were selected manually to obtain a global matching using Procrustes alignment (rotation + translation + scaling). This was done separately for the modern human (left) and fossil samples (right). Both samples were finally aligned by manually selecting the corresponding landmarks in the fossil and modern human sample (middle). (B): The region of interest is bounded by the mesial faces of the left and right

crowns of the deciduous or permanent canines and bounded superiorly by the base of the alveolar bone to exclude the teeth. (C): Illustration of automatic semi-landmark extraction.

2D: The endpoints of the midsagittal profile are located as the points with the smallest second spatial coordinate (x_2). N_L equidistantly distributed points along the curve are selected as

semi-landmarks. 3D: N_{L1} equidistant 2D slices are extracted, each containing a profile curve.

For each profile, N_{L2} semi-landmarks are extracted as explained above resulting in $N_{L1} \times N_{L2}$ semi-landmarks.

Table S1. Within-group variation. To compare the variation between the modern human populations (African vs. European), the within-group variation is calculated as $(N - 1) \cdot \sum_{i=1}^N (x_i - \bar{x})^2$ where N samples x_i belonging to group g are represented by their PC coordinates. Additionally, we report the difference between the within-group variation of the two groups in percentage and we tested the statistical difference of the within-group variation (difference of samples to their group mean) using an unpaired one-sided t-test and report the p-values. Populations: Modern humans, Modern humans* (African population without the six individuals between 11 and 16 years of age), All (modern humans and australopiths).

			Atlas		Pairwise	
			Profile	Surface	Profile	Surface
Modern humans	African	Within-	4.080	5.907	2.659	2.309
	European	Group var.	1.961	3.729	1.114	1.337
		%	108.09%	58.44%	138.69%	72.74%
		p-val.	< 0.001	< 0.01	< 0.001	< 0.01
Modern humans*	African	Within-	3.204	4.632	—	—
	European	Group var.	1.950	3.724	—	—
		%	64.28%	24.37%	—	—
		p-val.	<0.001	<0.01	—	—
All	African	Within-	3.861	5.522	2.810	2.383
	European	Group var.	1.812	3.471	1.148	1.364
		%	113.13%	59.09%	144.88%	74,71%
		p-val.	<0.001	<0.01	<0.0001	<0.01
	A. africanus	Within-	0.261	0.038	0.064	0.011
	P. robustus	Group var.	0.304	0.146	0.057	0.031

Video S1. Modern human sample. Plot of first three principal components obtained by kernel PCA using the atlas approach on the symphyseal surface.

Video S2. Modern human sample. Plot of first three principal components obtained by kernel PCA using the pairwise approach on the symphyseal surface.

Video S3. Modern human sample. Plot of first three principal components obtained by kernel PCA using the atlas approach on the midsagittal profile.

Video S4. Modern human sample. Plot of first three principal components obtained by kernel PCA using the pairwise approach on the midsagittal profile.

Video S5. Modern human sample. Visualization of shape differences captured in the midsagittal profile. Heatmaps on global mean shape show the point displacement (in mm) between groups.

Video S6. Modern human sample. Visualization of shape differences captured in the symphyseal surface. Heatmaps on global mean shape show the volume change (in %) between groups.

Video S7. Modern human and australopith sample. Plot of first three principal components obtained by kernel PCA using the atlas approach on the symphyseal surface.

Video S8. Modern human and australopith sample. Plot of first three principal components obtained by kernel PCA using the pairwise approach on the symphyseal surface.

Video S9. Modern human and australopith sample. Plot of first three principal components obtained by kernel PCA using the atlas approach on the midsagittal profile.

Video S10. Modern human and australopith sample. Plot of first three principal components obtained by kernel PCA using the pairwise approach on the midsagittal profile.

Video S11. Modern human and australopith sample. Visualization of shape differences captured in the midsagittal profile. Heatmaps on global mean shape show the point displacement (in mm) between groups.

Video S12. Modern human and australopith sample. Visualization of shape differences captured in the symphyseal surface. Heatmaps on global mean shape show the volume change (in %) between groups.